Real-time Raman spectroscopy measurements to study the uniaxial tension of isotactic polypropylene: a global overview of microstructural deformation mechanisms

J. Martin, M. Ponçot, J.M. Hiver, P. Bourson, A. Dahoun

▶ **To cite this version:**

J. Martin, M. Ponçot, J.M. Hiver, P. Bourson, A. Dahoun. Real-time Raman spectroscopy measurements to study the uniaxial tension of isotactic polypropylene: a global overview of microstructural deformation mechanisms. Journal of Raman Spectroscopy, 2013, 44 (5), pp.776-784. ⟨10.1002/jrs.4244⟩. ⟨hal-03612273⟩

HAL Id: hal-03612273

https://hal.univ-lorraine.fr/hal-03612273v1

Submitted on 31 Jan 2023

HAL is a multi-disciplinary open access archive for the deposit and dissemination of scientific research documents, whether they are published or not. The documents may come from teaching and research institutions in France or abroad, or from public or private research centers.

L'archive ouverte pluridisciplinaire **HAL**, est destinée au dépôt et à la diffusion de documents scientifiques de niveau recherche, publiés ou non, émanant des établissements d'enseignement et de recherche français ou étrangers, des laboratoires publics ou privés.

HAL Authorization

Real-time Raman spectroscopy measurements to study the uniaxial tension of isotactic polypropylene: a global overview of microstructural deformation mechanisms

J. Martin [1, 2], M. Ponçot[2], J.M. Hiver[2], P. Bourson[1*], A. Dahoun[2]

(1) Laboratoire Matériaux Optiques, Photonique et Systèmes, Université de Lorraine et Supélec, UMR CNRS 7132, 2 rue Edouard Belin, 57070 Metz, France

(2) Institut Jean Lamour, Département SI2M, UMR CNRS 7198, Nancy Université, Parc de Saurupt, 54011 Nancy, France

* Author to whom correspondence should be addressed

Abstract:

Micro-Raman spectroscopy was used to investigate the main deformation micro-mechanisms of isotactic polypropylene uniaxially stretched at constant temperature (T = 30 °C) under a constant true strain rate ($\dot{\varepsilon}_{zz} = 5.10^{-3}$ s^{-1}). To accurate measurements namely to be free of the recovering phenomenon which causes in most of the cases interference during *post-mortem* analysis, we introduced a new experimental set-up combining a Raman spectrometer with a tensile machine piloted by the VidéoTraction™ system. Microstructure is described by essential parameters such as the crystallinity index, the molecular orientation both in the crystalline and amorphous phase, distribution of the stress at the chemical bonds scale. For each, a well-tried Raman spectral criterion was used. Cross-checking of these results, obtained with a minimum of tensile tests, allows a more complete understanding of the deformation micromechanisms of semi-crystalline polymer.

Keywords :

Polymer; Deformation; Crystallinity index ; Molecular orientation ; Real-time

1. Introduction

Macroscopic properties of materials, such as the mechanical behaviour, are closely related to their microstructures[1] . In the case of semi-crystalline polymers, the crystallinity index and the molecular orientation in crystalline and amorphous phase are considered to be essential factors to understand this relationship and to optimise their end-use properties[1-3] . At the macroscopic scale, mechanical properties of such materials are determined on normalized sample shapes using conventional uniaxial tensile tests[4]. At the microscopic scale, a number of indirect analytical techniques can be used to investigate the microstructure such as thermal analysis, microscopic observations, X-ray scattering, birefringence and Nuclear Magnetic Resonance (NMR)[5-7]. By collecting both these macroscopic and microscopic data, numerous experimental works have attempted to associate one state of deformation (such as the strain level) to one state of microstructure (such as molecular orientation) in order to propose elementary descriptive models of the deformation micro-mechanisms[8-12]. A good review of these deformations mechanisms has been published by Bowden and Young[13] . In that vein, the papers of Peterlin[9] , focused on polyethylene and polypropylene, developed the first models showing how the crystalline structure are sheared, rotated and fragmented under uniaxial tension. Numerous studies have improved existing models by introducing the metallurgical concept of dislocation and glide systems involving slip within the lamellar crystals during the yielding[14-16]. Contribution of amorphous phase was then introduced by Treloar et al.[17] , Young et al.[18] and Bartczak et al.[19] and then computed by Van der Giessen et al.[20] and G'Sell et al.[21] by considering a composite approach of the material. Central role of tie molecules localized in the interlamellar layers in determining viscoelastic, plastic deformation, and failure was evidenced in pioneering works by Nitta and Takayanagi[22, 23] . However, in many cases, evidence of these mechanisms is debatable for two major experimental limits. i) In the case of ductile materials which experience a pronounced necking

due to their plastic instability (such as polymers), conventional mechanical tests used widely by the past and giving access to the nominal stress – strain curve are inappropriate to reveal their intrinsic mechanical behaviour at prescribed temperature and strain rate[24] . In order to perform quantitative measurements, geometry variations in the necking zone of the stretched sample have to be taken into account along the entire course of the tensile test[25, 26]. ii) Furthermore, conventional analytical techniques suffer from a common difficulty related to their rather elaborate instrumental set-up, often costly and bulky, which requires in most of the cases *post mortem* analysis and destructive sampling procedure coupled with serious risks of structural damage. For accurate measurements, one has to consider the microstructural evolution in real-time with the deformation especially to avoid the material recovering which occurs after sample unloading[17, 27-29]. The main purpose of this work is thus to overcome these two experimental difficulties by coupling two original experimental instruments:

i) On the one hand, by using a video-controlled testing device (called VidéoTraction™), developed in our laboratory by G'Sell and Hiver[30-32] , the true constitutive mechanical behaviour of semi-crystalline polymers is determined under a constant true strain rate by taking into account the plastic instability of the polymer which occurs during de deformation.

ii) On the other hand, a Raman spectrometer is coupling to the tensile test machine allowing in situ acquisitions. Due to its recent instrumental improvements in particular the advent of laser radiations and the development of Couple Charge Device (CCD) detectors, Raman spectroscopy is adapted for polymer microstructure characterization with reliability, rapidity and commodity[33-35]. It gives access to the vibrational frequencies of the covalent chemical bonds of polymers and allows analysis of molecular species at different scales, from the chemical repetitive unit to the conformational architecture of the macromolecular chain[36, 37] .

In this paper, we propose to apply this experimental set-up in a practical application e.g. to follow the microstructural evolution of an isotactic polypropylene in real-time with its uniaxial stretching over a large true strain range, from the elastic to the stress hardening deformation domains. Major microstructural features are considered such as the crystallinity index, the molecular orientation (both in crystalline and amorphous phase) and the stress distribution at the chemical bonds scale. On this point, Colomban et al.[38, 39] report some valuable *in situ* results performed on polyethylene terephtalate (PET), polyamide 66 (PA66) and isotactic polypropylene (iPP). However these investigations are based on the low-wavenumber spectral range of the Raman spectrum (collective modes) and the deformation domain under consideration was limited to the viscoelastic response of the polymers. Moreover numerous studies relating Raman spectroscopy *in situ* measurements deal with the stress-induced Raman wavenumber shifts[40-43] but only few papers about Raman bands intensity[44, 45] .

On the basis of previous elementary descriptive models, our results are principally discussed in terms of deformation micro-mechanisms explaining relationship between the polymer mechanical behaviour and its microstructure.

2. Experimental details

2.1 Material

The investigated polypropylene was manufactured by Atochem under the reference 3050 MN1. This natural isotactic grade is characterized by a relatively broad molecular weight distribution, as assessed by gel permeation chromatography, with $\overline{M}_w$ = 262000 g.mol^{-1} and $\overline{M}_n$ = 75900 g.mol^{-1}. Pellets of the polymer were subsequently processed by injection-molding into 4 mm thick plates (Apollor, Lunéville, France). The density of the material is firstly determined by hydrostatic weighting, ρ = 0.916 g.cm^{-3}. Based on density values published in the literature for perfectly crystalline and amorphous phase (ρ_c = 0.946 g.cm^{-3}

and ρ_a = 0.854 g.cm^{-3}, respectively[46]), the weight index of crystallinity, $<X_c>$, is found to be equal to 67 %. This value is confirmed by Differential Scanning Calorimetry (DSC) measurements performed at a heating rate of 10 °C.min^{-1} showing a melting point located at T_m = 165 °C with an enthalpy of fusion, ΔH_m, equal to 109J.g^{-1}. This corresponds to a weight index of crystallinity of about 66 % (the theoretical enthalpy of fusion considered for a perfect crystal of infinite size, $\Delta H_{t,m}$ is 165 J.g^{-1})[46]. The glass transition temperature, T_g, is measured at 5 °C.

X-ray scattering measurements obtained with a Bruker AXS (ref. D8 Advance) equipped with a Cu-K$_{\alpha 1}$ ($\lambda_{CuK\alpha 1}$ = 0.1542 nm) Johansson monochromator proves the semi-crystalline nature of the investigated iPP. The narrow peaks located at 2θ = 14.1, 16.9, 18.5, 21.2 and 21.8 degrees evidences the presence of the α-monoclinic form of the iPP crystals because they are due to the selective diffraction of the (110), (040), (130), (111) and ($\bar{1}$31) crystallographic planes of the α-monoclinic unit cell respectively[47] . The spherulitic morphology is observed by means of polarized optical microscopy performed on thin slices (20 µm thickness). Observations show spherulites of about 55 µm average diameter.

2.2 Experimental set-up and samples

To follow evolution of the iPP microstructure in real-time with its uniaxial deformation, we customized a system coupling a video-controlled tensile machine with a Raman micro-spectrometer. A schematic view of this experimental set-up are displayed inref. 56.

The video-controlled mechanical testing method used here is the latest version of the VidéoTraction™ system developed by G'Sell and Hiver[30] . This device provides direct access to the true mechanical behaviour of polymers under uniaxial tension at prescribed temperature, T, and strain rate, $\dot{\varepsilon}_{zz}$, up to very large levels of deformation, even plastic instabilities (necking) appear. Along the entire course of a tensile test, geometry instabilities

localized in the necking zone of the polymer sample are taken into account by video measurements. The VideoTraction™ system, widely described in previous papers by G'Sell et al.[31, 32] and Addiego et al.[48] , is composed of a servo-hydraulic testing machine (MTS 810) and a video CCD camera. Both are interfaced with a microcomputer equipped with an image-digitalizing card. During the tensile test, the microcomputer receives simultaneously two kinds of information: i) the applied force recorded by a load cell, and ii) the image of ink markers (points) printed in a predefined local material element termed as the Representative Volume Element, RVE. The **z**-axial and the **x**-transversal true strains, noted ε_{zz} and ε_{xx} are calculated in real-time by image analysis from the axial and transversal displacements of the markers. The **y**-transversal true strain, noted ε_{yy}, is deduced from the **x**-one, ε_{xx}, by considering the transversal isotropy of the strain field in the center of the neck, $\varepsilon_{yy} = \varepsilon_{xx}$. The axial true stress (Cauchy stress), σ_{zz}, is also determined in the RVE by taking into account the cross-section reduction during the tensile test. Finally, the hydraulic ram velocity is automatically servo-controlled in such a way that the local true strain rate $\dot{\varepsilon}_{zz}$ in the RVE is maintained constant during the tensile test.

Raman spectra are collected in backscattered geometry using an iHR250® spectrometer developed by Horiba Jobin Yvon (Lille, France) linked to a remote head of probe by means of two optic fibres: one fibre for sending the incident radiation to the sample and the second one for collecting and sending the backscattered radiation to the spectrometer. The head of probe, placed in face to face to the video-controlled system, is equipped with an Olympus long working distance objective lens (x 50 as objective length, x 500 as total magnification, 12 mm as focal distance). Laser radiation coming from a diode laser, producing a λ = 785 nm wavelength radiation, is maintained focused onto the flat surface in the predefined RVE zone of the test sample where necking is expected. At maximum laser power (300 mW), the probe typically delivers an illumination power density of about 15 mW.μm^{-2}. The head of probe is

also equipped with a linear polarizer and analyser which allow polarizing the incident laser beam and the Raman scattering radiation, respectively. Rayleigh scattered light is eliminated through a holographic Notch filter placed on the light path just before the diffraction grating (1200 grooves.mm^{-1}). The spectral resolution achieved is about 0.5 cm^{-1}. Previously, the Raman shift is calibrated using a reference sample of pure silicon which shows a well reported scattering band at 521 cm^{-1}. A micro-computer interfaced with the spectrometer allows recording raw spectra by means of the Labspec® acquisition software (Horiba Jobin Yvon, Lille, France). A self-written fitting least-square procedure based on the Levenberg-Marquardt method is used to process raw data[49] . Residual fluorescence background is eliminated by a polynomial baseline cutting procedure. A mixed Gaussian-Lorentz function is used to decompose each scattering band and the final adjustment gives access to the useful spectral features such as position, ν (cm^{-1}), integrated intensity, I (a.u), and full width at half maximum, FWHM (cm^{-1}).

The test specimens are machined out from the injection-molded plates using a computer-controlled milling machine (CharlyRobot CRA4) following a thin film geometry as described in ref. 56.. Thickness is considerably reduced from 4 mm to 500 µm (by polishing flate surfaces) in order to obtain a film geometry. Main reason is to minimize the deflection of the necking zone to ensure a suitable focalisation of the laser onto the sample all along the mechanical test.

All specimens are stretched at T = 30 °C under a constant true strain rate $\dot{\varepsilon}_{zz}$ = 5.10^{-3} s^{-1} until their rupture at ε_{zz} = 1.6. During the entire course of the tensile test 40 Raman spectra are recorded. For each Raman spectrum, acquisition time is fixed at 5 s. . Note that results are based on the repetition of 10 tensile tests in exactly the same experimental conditions in order to ensure reproducibility.

2.3 Measurement procedures

To describe microstructure of iPP under deformation, 4 microstructural features are considered such as i) the cristallinity index, ii) the orientation of macromolecules in the crystalline phase, iii) the orientation of macromolecules in the amorphous phase, iv) the distribution of stress at the chemical bonds scale. For each, we adopted a particular Raman spectral criterion developed in our previous study[51-56] on the basis of fundamental works on vibrational mode assignments[57-61]. Table 1 summarized the vibrational mode assignments and the phase belonging (crystalline and/or amorphous) of the Raman scattering bands used to design theses spectral criterions.

The crystallinity, index noted $<X_c>$, is deduced from depolarized Raman spectroscopy measurements by determining the criterion $R_c = (I_{809}+I_{842}) / (I_{835}+I_{809}+I_{842})$ of integrated intensity of scattering bands located at 809 (60 % crystalline), 835 (0 % crystalline) and 842 cm^{-1} (65 % crystalline) (Table 1). Due to the fact that bands at 809 and 842 cm^{-1} are not pure crystalline bands, we proposed in a previous study to adjust R_c by balancing factors in order to estimate $<X_c>$ according to the following matching relation :

$$< X_c > = 0.81\, R_c + 0.01 \qquad (1)$$

The molecular orientation is estimated from Raman spectroscopy by performing measurements in a particular polarization geometry of the incident and scattered radiations noted x(zz)x (as Porto's notation[62]) where both the incident and scattered radiations are polarized along the z-stretching direction. In these conditions, we demonstrate in previous papers that the ratio $R_{orient,c} = I_{973} / I_{998}$ of the integrated intensity of the two particular Raman scattering bands at 973 (symmetric stretching mode of the C-C skeletal backbones in crystalline phase) and 998 cm^{-1} (rocking mode of CH_3 lateral alkyl groups in crystalline phase), enable to estimate orientation of crystalline phase chains in the **z**-tensile direction. In

uniaxial tension, G'Sell and Dahoun[63] show the development of a fiber texture which can be characterized by the determination of only one orientation function, $F_{\mathbf{c/z}}$, describing the spatial distribution of the crystallographic **c**-axis towards the **z**-tensile direction. A matching relation between $R_{orient,c}$ and $F_{\mathbf{c/z}}$ was established as follow :

$$F_{\mathbf{c/z}} = 0.135\, R_{orient,c} - 0.18 \qquad (2)$$

Keeping the same polarization configuration, x(zz)x, we used the ratio $R_{orient,am} = I_{835} / I_{tot}$ of the unique band at 835 cm^{-1} (stretching mode of the C-C skeletal backbones in amorphous phase) as a spectral criterion of amorphous chains orientation . I_{tot} is the integrated intensity of the entire recorded spectrum. By the same reasoning, a linear relation was established between $R_{orient,am}$ and orientation function of the amorphous phase $F_{\mathbf{am/z}}$ describing the spatial distribution of amorphous macromolecules towards the **z**-tensile direction .

$$F_{\mathbf{am/z}} = 14.4\, R_{orient,am} - 1 \qquad (3)$$

The position dependence of Raman bands versus applied stress, commonly called stress-induced Raman shifts, is of fundamental importance in understanding how a macroscopic stress is distributed at the chemical bonds scale[41-43]. These wavenumber shifts are interpreted on the basis of the anharmonicity of chemical bonds, stress inducing an interatomic distance alteration which changes the atomic vibration frequencies[39]. Shifts are expected different according to the nature of the chemical bonds and their orientation towards the macroscopic applied stress direction. A shift towards the low wavenumbers means that bonds are under an extension stress while a shift towards the high ones is related to a compressive stress. In a depolarized configuration, we proposed to follow the normalized shift evolution,

$R_s^{809}=\nu_{809}/\nu^0_{809}$, $R_s^{835}=\nu_{835}/\nu^0_{835}$ and $R_s^{842}=\nu_{842}/\nu^0_{842}$ of bands at 809, 835 and 842 cm^{-1} in function of the true axial strain ε_{zz}. ν^0_{809} is the reference position of the 809 cm^{-1} band reported for no applied stress. Objective is to explore the evolution of stress distribution both in crystalline (809 and 842 cm^{-1}) and amorphous phase (835 cm^{-1}) during the deformation.

3. Results

3.1 Mechanical behaviour

Uniaxial tension of the iPP was performed at T = 30 °C remaining a constant axial true strain rate $\dot{\varepsilon}_{zz} = 5.10^{-3}\ s^{-1}$. Evolution of the true axial stress – strain curve ($\sigma_{zz} - \varepsilon_{zz}$) is presented in ref. 56. Three different stages are noted. The first one, $\varepsilon_{zz} = 0 - 0.09$, corresponds to the elasto-viscoelastic behaviour of the iPP. The initial slope of the curve corresponds to the elastic Young's modulus, E = 1.7 GPa. The yield point is defined when stress σ^y_{zz} achieves 36 MPa and passes through a round-off maximum at strain $\varepsilon^y_{zz} = 0.09$. The second stage, $\varepsilon_{zz} = 0.09 – 0.8$, corresponds to the soft-plastic deformation. At the beginning, stress is marked by a small but significant stress decrease while the deformation localizes in a sharp neck in the RVE (structural softening). This is then followed by a symmetric propagation of the neck shoulders towards the specimen heads at almost constant stress, $\sigma_{zz} = 32$ MPa (easy plastic flow). The last stage, $\varepsilon_{zz} = 0.8 – 1.6$, termed as the plastic stress-hardening regime, shows a nearly exponential increase of the stress from 32 to 71 MPa.

3.2 Cristallinity index

Figure 1 shows fitted Raman spectra recorded in the useful spectral range 780 – 860 cm^{-1} at growing true axial strain level, $\varepsilon_{zz} = 0$, 0.1, 0.8 and 1.4. Intensity of bands at 809 and 842 cm^{-1}, which are characteristics of the crystalline phase, decreases regularly with the increasing deformation. On the contrary, intensity of one at 835 cm^{-1}, exclusively associated to the amorphous phase, increases with the increasing deformation. This observation evidences

qualitatively a loss of crystallinity in iPP with deformation, chains initially present in the crystalline phase going through the amorphous one. On the same figure, we note shifts of bands. This point will be discussed further in details. Figure 2 presents evolution of the crystallinity index of iPP, $<X_c>$, versus the axial true strain, ε_{zz}. It confirms the general decrease of the crystalline phase amount with the increasing deformation. Evolution marked a three-stage behaviour with the true axial strain, ε_{zz}: i) in the elasto-viscoelastic regime, from 0 to 0.09, the crystallinity index is high and quite constant, $<X_c> = 0.67$, ii) then drops drastically in the soft-plastic deformation regime, from 0.09 to 0.8, passing from $<X_c> = 0.67$ to 0.57 and iii) finally decreases softly in the stress-hardening regime, from 0.8 to 1.6. Just before the rupture, the crystallinity index is low and equal to $<X_c> = 0.54$.

3.3 Orientation of macromolecules in the crystalline phase

Figure3reports fitted Raman spectra recorded in polarized configuration, **x(zz)x**, at growing true axial strain level, ε_{zz} = 0, 0.1, 0.8 and 1.4. The spectral range under consideration, 950 – 1010 cm^{-1}, includes the useful scattering bands at 973 and 998 cm^{-1} required for estimating orientation of chains in the crystalline phase. Intensity of the band at 973 cm^{-1} (symmetric stretching mode of the C-C skeletal backbones) increases with the increasing strain. This corresponds to an increasing proportion of C-C skeletal backbones oriented in the **z**-polarization direction which is also the **z**-stretching axis. Just the opposite is observed for band located at 998 cm^{-1} (rocking mode of the CH_3 lateral alkyl groups) because number of CH_3 lateral groups becomes lower in the z-stretching direction. Figure 4 shows the evolution of the orientation function of the crystalline phase, $F_{c/z}$, and the true axial stress σ_{zz} in function of the true strain ε_{zz} from 0 to 1.6. Increasing evolution of $F_{c/z}$ with deformation is consistent with a gradual orientation of crystalline chains towards the z-tensile direction and can be described into three major domains with respect to the true axial strain, ε_{zz}: i) In the elasto-viscoelastic regime, from 0 to 0.09, $F_{c/z}$ is low and quite constant, $F_{c/z}$ = 0.05. It

indicates that crystalline chains are still randomly oriented in the material. ii) In the soft-plastic deformation regime, $F_{\mathbf{c/z}}$ increases gradually from 0.05 to 0.48. This is related to the beginning of the crystalline chains orientation towards the z-tensile direction. We can note that the inflection point of the increasing evolution of the orientation function is localized at nearly $\varepsilon_{zz} = 0.85$, $F_{\mathbf{c/z}} = 0.36$. It suggests that the orientation mechanisms of crystalline chains take a predominant place for this particular strain level. iii) In the last stress-hardening regime, $F_{\mathbf{c/z}}$ is still increasing but its progression becomes milder. Approaching the fracture, $F_{\mathbf{c/z}}$ is maximal and quite constant $F_{\mathbf{c/z}} = 0.74$ suggesting that crystalline chains have almost achieved their maximal orientation level before the material rupture.

3.4 Orientation of macromolecules in the amorphous phase

Figure 5 shows fitted Raman spectra recorded in polarized configuration, **x(zz)x**, at growing true axial strain level, $\varepsilon_{zz} = 0$, 0.1, 0.8 and 1.4. In the spectral range considered, 780 – 880 cm^{-1}, is only plotted the useful polarized scattering band at 835 cm^{-1} which allows calculation of the orientation function of the amorphous chains $F_{am/\mathbf{z}}$ taking the **z**-tensile direction as reference. Intensity of this band increases simultaneously with the deformation. This observation is interpreted by considering both the chemical bond associated to this scattering band e.g. the symmetric stretching mode of the C-C skeletal backbones in the amorphous state and the polarization direction. An increasing intensity evidences an increase of C-C bond proportion oriented parallel to the **z**-polarization direction which is also the stretching direction. Thus, chains of amorphous phase tend to be preferentially oriented along the **z**-tensile direction. Figure 6 presents the evolution of the orientation function of the amorphous phase $F_{\mathbf{am/z}}$, and the true axial stress σ_{zz} in function of the true strain ε_{zz} from 0 to 1.6. Increasing evolution of $F_{\mathbf{am/z}}$ with deformation confirms our preliminary observations: macromolecular chains tend to be oriented towards the **z**-tensile direction. It can be delimited with respect to the true axial strain, ε_{zz}: i) In the elasto-viscoelastic regime, from 0 to 0.09,

chains are profoundly affected by the deformation since $F_{am/z}$ raises from 0.03 to 0.3. ii) In the soft-plastic deformation regime, from 0.09 to 0.8, orientation of amorphous is milder passing from $F_{am/z}$ = 0.3 to 0.6 and iii) becomes more and more moderate $F_{am/z}$ = 0.6 – 0.7 in the stress-hardening regime, from 0.8 to 1.6. Approaching the fracture deformation, $F_{am/z}$ exhibits a maximal and quite constant value, $F_{am/z}$ = 0.7, suggesting that amorphous chains have almost achieved their maximal orientation level before rupture.

3.5 Stress distribution

In figures 1 and 3 we have noted that bands at 809, 835 and 841 cm^{-1} exhibit opposite wavenumber shifts with deformation. Bands at 809 and 835 cm^{-1} possessing both a high contribution of the C-C skeletal backbones moves towards lowwavenumbers. This indicates that these chemical bonds experience an increasing extension stress with the increasing deformation as described by. On the contrary, crystalline band at 842 cm^{-1}, principally attributed to the CH_2 lateral groups, moves up to highwavenumbers. This evidences the compressive solicitation that endures C-H lateral bonds during stretching. These observations are in good agreement with previous studies of Wool et al.[64] in case of polyethylene. Figure 7 shows evolution of the normalized position, ν/ν^0 of the crystalline bands at 809 and 842 cm^{-1} whereas figure 8 plots the amorphous one at 835 cm^{-1}. ν^0 represents position of bands for the non-deformed iPP. Despite that shift of crystalline bands at 809 and 842 cm^{-1} have an opposite behaviour, their evolutions are comparable in function of the true axial strain, ε_{zz}: i) In the elasto-viscoelastic regime, from 0 to 0.09, normalized shifts of both bands are very low. This indicates that application of extension-stress on the C-C skeletal backbones and compressive-stress on C-H lateral bonds is weak as if crystalline chains are not yet regarded by the deformation. ii) In the soft-plastic deformation regime, from 0.09 to 0.8, positions of bands move gently meaning that stress is progressively applied on chemicals bonds. ii) In the last stress-hardening regime, from 0.8 to 1.6, bonds are strongly constrained since shifts

exhibit important variations. By comparing evolution of the extension-stress on C-C bonds between crystalline (Figure 7) and amorphous chains (Figure 8), we note major differences particularly in the elasto-viscoelatic regime where amorphous C-C bonds are highly constrained while crystalline ones are not yet affected.

4. Discussion

Discussion will turn to the description of the deformation micro-mechanisms occurring in the semi-crystalline structure of iPP by clearly discerning the three different regimes of the mechanical behaviour, i) elasto-viscoelastic regime, ii) soft-plastic regime and iii) stress-hardening regime. It will be based on the cross-checking of the results obtained previously and summarized in Table 2. Such a rigorous description has to take into account two special crystal features of the α-iPP spherulites. : i) The high dependence of the initial orientation of lamellae, distributed in equatorial, diagonal and polar regions of the spherulite, with respect to the macroscopic applied stress **z**-direction[65]. ii) The cross-hatch type lamellar branching which exhibits radial ("mother") and tangential ("daughter") lamellae oriented nearly orthogonally[47]. Radial lamellae correspond to the $\mathbf{c_1}$-crystallographic axis and the tangential ones to the $\mathbf{c_2}$-axis. This last point explains strongly the mechanical behaviour differences observed with the β-iPP spherulites which consist of broad, locally stacked radial lamellae, just as in spherulites of polyethylene[66, 67]. Under tensile loading, it has been shown that the α-iPP spherulites exhibit brittle behaviour whereas the β-ones deform plastically with little damage (occurrence of cavitation) up to strain of about $\varepsilon_{zz} = 0.25$.

4.1 Elasto-Viscoelastic regime

In the elasto-viscoelastic regime (Figure 9), $\varepsilon_{zz} = 0 – 0.09$, results demonstrate that it is only the amorphous phase which plays a major role in the deformation process: orientation of amorphous chains is high and accompanied by the application of an important extension-

stress level on the amorphous C-C skeletal backbones. On the contrary, deformation mechanisms involving crystalline phase are not yet active: neither the crystalline chains orientation nor the crystallinity index change. This is usually explained by considering the soft amorphous phase behaviour compared with the rigid crystalline blocks. In the analogous case of polyethylene, Schultz et al.[10] show that the nanoscopic elastic modulus of one chain is sixteen times higher than the macroscopic one evidencing the essential contribution of the soft amorphous phase. For $T > T_g$, the Van der Waals interactions are overcome and the amorphous part exhibits a rubber-like behaviour. Initially under an interpenetrating coils configuration, chains in the interlamellar layers have enough molecular mobility to orient themselves towards the **z**-tensile direction in order to accommodate the deformation. It involves disentanglement, extension and alignment of tie molecules between two adjacent crystalline lamellae. This is particular true for stacked lamellae oriented perpendicularly to the stretching direction such as for the radial and tangential ones in equatorial and polar regions respectively. Adjacent lamellae are separated and the average length of the amorphous interlamellar layer increases[13] . The important extension-stress measured on the amorphous C-C skeletal backbones is in good agreement with this interpretation. On the contrary, lamellae in polar regions undergo locally a compressive stress leading to move lamellae closer. Amorphous chains are confined in the interlamellar layer. Radial and tangential lamellae in diagonal regions, inclined at $\pm$ 45 ° with respect to the macroscopic **z**-tensile direction are locally subject to a shear stress which promotes lamellae sliding. This leads to a progressive extension and alignment of amorphous chains. Deformation of amorphous phase is always at least partially reversible in the elastic domain and time-dependent in the viscoelastic one[17, 18] . This is due to the thermodynamic tendency of the stretched chains to return to their coiled geometry.

4.2 Soft-plastic deformation regime

In the soft-plastic deformation regime (Figure 9), ε_{zz} = 0.09 – 0.8, results show that orientation of the crystalline chains towards the **z**-tensile direction is dominant, the crystallinity index drops drastically, the macroscopic stress is more and more disseminated on the chemical bonds of the crystalline macromolecules and the volume damage is activated. These important changes noted for the crystalline phase signal clearly the activation of new deformation mechanisms differing from these encountered during the viscoelastic regime. After a critical stress is achieved corresponding to the yield point, amorphous phase cannot accommodate any more the increasing deformation because interlamellar extension and/or shearing process is limited by the finite extensibility of the highly entangled chains (or tie-molecules). Therefore these are crystals which are affected at their turn by dissipative deformation mechanisms as plastic flow and formation of micro-voids in the amorphous layers and / or at inter-spherulitic boundaries[13] . In the true stress – strain curve of iPP, the stress drop occurring just past the yield point, is caused by the catastrophic and cooperative failures of the lamellae accompanying deformation. In the equatorial regions, Nitta and Takayanagi[22, 23] proposed that tie molecules between two adjacent lamellae support the external force and produce locally a concentrated load on lamellae surfaces leading to the lamellae bending, as shown in figure 9. They show that under a critical bending stress value, calculating as a function of the tie molecules fraction, lamellae are break up into smaller blocks. In parallel, our results on crystallinity show that a part of crystalline chains is pulled-out from the folded-chains lamellae. This is commonly termed as the mechanically-induced melting process. At the same time, micro-voids appear in the amorphous layers where density of tie-molecules is lower, and transform progressively into cavities with the increasing deformation[12] . In polar regions, the existence of a local compressive stress induces also a lamellar bending in the meaning of Nitta and Takayanagi[22, 23]. Crystal blocks are at first pulled out of the lamellae, then rotate towards the z-tensile axis and are subject in part to

disintegration[10] . Deformation mechanisms in diagonal regions are quite different since radial and tangential lamellae are oriented at ± 45 ° versus the **z**-tensile axis which promotes fine crystallographic slips by generation and glide of dislocations leaving the lamellae intact[15, 16] . In uniaxially stretched isotactic polypropylene, it was demonstrated that minimum value of the Critical Resolved Shear Stress (CRSS) is firstly achieved for chain slip mode along the (100)[001], (010)[001], (110) [001] and ($\bar{1}$10)[001] glide systems[63] . For further deformation, this crystal plasticity, that readily accommodates most of the applied deformation, leads to consecutives secondary effects such as i) plastic tilt of crystallites towards the **z**-tensile axis, ii) lamellae fragmentation owing to coarse slip process, iii) crystalline phase destruction by chains pull-out process and iv) micro-voids formation in the amorphous layers[8-13] . On this last point, it is worth to note that voiding appears earlier in the equatorial and polar regions of the spherulites where plastic slip is less favourable compared to the diagonal ones. These interpretation were assessed by previous microscopy studies on the transition from yielding to crazing in polypropylene concluding to a competition between crystal slip and voiding in governing the propagation of cavitation across the spherulite[68] . In addition, the fact that voids occur at the same time in the equatorial and polar regions is related to the cross-hatched structure of the α-iPP spherulites and gives credit to the assumption that radial lamellae in equatorial position deformed similarly as the tangential ones in the polar regions and *vice-versa*. In the case of polyethylene and polybutene which present both only radial lamellae, Addiego et al.[48] and Weynant et al.[69] show respectively, that the structural damage occurs firstly in the equatorial regions and long after in the polar ones.

4.3 Strain hardening regime

In the last strain-hardening domain (Figure 9), ε_{zz} = 0.8 – 1.6, results show principally that deformation mechanisms involving crystalline and amorphous phase become stable: orientation of the crystalline and amorphous chains is less active, the loss of crystallinity slow

down and volume strain achieves practically its maximum level. This means that mechanisms of plastic deformation are depleted and the initial isotropic lamellar structure is transformed into a highly anisotropic and damaged micro-fibrillar structure oriented towards the tensile direction[13] . Contrary to the soft-plastic regime, deformation mechanisms in the strain-hardening one are quite identical in the equatorial, diagonal and polar regions of the α-iPP spherulite as illustrated in figure 9. The microstructure accommodates the continuing deformation only by the extension and the valence angle opening of the chemical bonds. The force required for displacing the C-C bonds from their equilibrium distance (related to the Morse's potential) is such important that the stress increases drastically in this last deformation regime. Our results showing important variations of the local stresses at the chemical bonds assesses this interpretation: C-C skeletal backbones of both the crystalline and amorphous macromolecules are more and more under extension since they are oriented in the tensile direction. In contrast, the C-H lateral bonds are more and more compressed since they are practically oriented towards the compressive direction of the uniaxial stress tensor. At large deformations, the ellipsoidal geometry of the voids observed in numerous microscopy studies is directly related to the application of a dilatation and a compaction stress (hydrostatic stress) along the axial and transversal directions, respectively. Approaching the polymer rupture, crystalline and amorphous chains have achieved their maximal orientation level, the proportion of crystalline phase is low and degraded in favour of the amorphous one, microstructure is highly damaged by the generation of crazes resulting from the nucleation, growth and coalescence of micro-voids (cavity). When chemical bonds cannot support the applied stress anymore, rupture of the polymer occurs by the rapid propagation of a crack (having a critical size) breaking craze fibrils as it grows[70] .

5. Conclusion

The deformation mechanisms of isotactic polypropylene during its uniaxial tension were investigated at the macroscopic scale by means of a 2D video extensometer (VidéoTraction^{TM}) giving access to the intrinsic stress – strain curve of the polymer for a constant true strain rate at constant temperature, and at the microscopic scale by micro-Raman spectroscopy. The new combination of these both techniques was introduced in this work and allows characterizing microstructure in real-time with its deformation by being free of the undesirable effects of the microstructure relaxation widely observed during *post-mortem* analysis. By this means, we demonstrate that rapidity of the spectral acquisitions presents a particular advantage in performing time-resolved measurements such as to follow the deformation mechanisms step by step. On the basis of the use of simple but reliable (previously validated) Raman spectral criterions appropriated for crucial features of the iPP microstructure (crystallinity index, chains orientation of both amorphous and crystalline phase and volume strain), we described evolution of the iPP microstructure in a large deformation domain from its elastic response to its rupture. Deformation of the spherulite microstructure results from a number of mechanisms involving both amorphous and crystalline phase. Such mechanisms are highly dependent on the orientation of structural elements with respect to the stress axis (equatorial, diagonal and polar regions). Results evidence clearly the transformation of the initial isotropic lamellar structure into a highly anisotropic and damaged micro-fibrillar structure oriented towards the stress direction. The main results show:

- the major role played by the amorphous phase during the initial elasto-viscoelastic deformation regime leading to interlamellar and / or shearing mechanisms.
- the major role played by the crystalline phase during the soft-plastic deformation regime such as crystal plasticity (for diagonal regions), lamellae destruction owing to a chains pulling-out mechanism, crystal tilting towards the stress direction, fragmentation, and voids generation,

- the major role played by the chemical bonds in resisting to the deformation during the last strain-hardening regime.

Further works should be devoted to a closer examination of the amorphous and crystalline phase evolution during loading and unloading cycles in order to have a better understanding of structural mechanisms occurring in the material relaxation.

References

1. I.M. Ward, *Mechanical Properties of Solid Polymers*, Wiley-Interscience, London (1971).

2. R.J. Samuels, *Structured Polymer Properties: The Identification, Interpretation, and Application of Crystalline Polymer Structure*, John Wiley & Sons, New York (1974).

3. R.J. Young and P.A. Lovell, *Introduction to Polymers*, Chapman & Hall, New York (1981).

4. C. G'Sell, In *Plastic Deformation of Amorphous and Semi Crystalline Materials*, B. Escaig and C. G'Sell, Les Editions de Physique, Les Ullis, 13-25 (1982).

5. B. Wunderlich, *Macromolecular Physics: Crystal Structure, Morphology, Defects*, Academic Press, New York (1973)

6. U.W. Gedde, *Polymer Physics*, Kluwer Academic Publishers, Dordrecht (1995)

7. A.J. de Vries, In *Plastic Deformation of Amorphous and Semi Crystalline Materials*, B. Escaig and C. G'Sell, Les Editions de Physique, Les Ullis, 329 - 344 (1982).

8. I.L Hay, *Kolloid ZuZ Polym. Band*, 204, 43-47 (1965)

9. A. Peterlin, *J. Mater. Sci.*, **6**, 490-508 (1971).

10. J. Schultz, *Polymer Materials Science*, Printice-Hall, Englewood Cliffs (1974).

11. J. Petermann, W. Kluge, H. Gleiter, *J. Polym. Sci*., 17, 1043 (1979).

12. K. Friedriech, In *Advances in Polymer Science, Crazing in Polymers 52/53*, H.H. Kausch, Springer-Verlag, Berlin-Heidelberg (1983).

13. P.B. Bowden, R.J. Young, *J. Mater. Sci*., 9, 2034-2051 (1974).

14. H. Gleiter, A.S. Argon, *Phil. Mag*., 24, 71 (1971)

15. A. Keller, D.P. Pope, *J. Mater. Sci.*, 6, 453-478 (1971)

16. L. Lin, A.S. Argon, *J. Mater. Sci.*, 29, 294 – 323 (1994)

17. L.R.G. Treloar, *The Physics of Rubber Elasticity*, Clarendon, Oxford (1975).

18. R.J. Young, P.B. Bowden, J.M. Ritchie, J.G. Rider, *J. Mater. Sci.*, **8**, 23-26 (1973)

19. Z. Bartczak, A. Galeski, A.S. Argon, R.E. Cohen, Polymer, 37, 2113-2123, (1996)

20. P.D. Wu, E. Van der Giessen, *Mech. Res. Comm.*, **19**, 427-433 (1992)

21. C. G'Sell, A. Dahoun, *Mat. Sci. Eng.*, **175**, 183-199 (1994)

22. K.H. Nitta, M. Takayanagi, *J. Polym. Sci*., **37**, 357-368 (1999)

23. K.H. Nitta, M. Takayanagi, *J. Polym. Sci*., **38**, 1037-1044 (2000)

24. C. G'Sell, In *Plastic Deformation of Amorphous and Semi Crystalline Materials*, B. Escaig and C. G'Sell, Les Editions de Physique, Les Ullis, 375-389 (1982).

25. C. G'Sell and J.J. Jonas, *J. Mater. Sci.*, **14**, 583-591 (1979).

26. C. G'Sell, N.A. Aly-Hellah and J.J. Jonas, *J. Mater. Sci*., **18**, 1731-1742 (1983).

27. R.H. Boyd, *Polymer*, **26**(3), 323-347 (1985).

28. C. Jourdan, J.Y. Cavaille and J. Perez, *J. Polym. Sci.*, **27**, 2361-2384 (1989).

29. B. Escaig, In *Plastic Deformation of Amorphous and Semi Crystalline Materials*, B. Escaig and C. G'Sell, Les Editions de Physique, Les Ullis, 187-225 (1982).

30. C. G'Sell and J.M. Hiver, French Patent #010542100, Bull. Off. INPI, 23 April: 2001.

31. C. G'Sell, J.M. Hiver, A. Dahoun and A. Souahi, *J. Mater. Sci.*, **27**, 5031-5039 (1992).

32. C. G'Sell, J.M. Hiver and A. Dahoun, *Int. J. Solids Struc.*, **39**, 3857-3872 (2002).

33. D.L. Gerrard and W.F. Maddams, *Appl. Spec. Rev*., **22**, 251-334 (1986).

34. S.J. Spells, In *Characterization of Solid Polymers: New Techniques and Developments*, S.J. Spells, Chapman & Hall, London (1994).

35. G. Xue, *Prog. Polym. Sci.*, **19**, 317-388 (1994).

36. J.L. Koenig, *Spectroscopy of Polymers*, 2nd edition, Elsevier Science, New York (1999).

37. D.I. Bower, W.F. Maddams, The Vibrational Spectroscopy of Polymers, Cambridge University Press, Cambridge (1989).

38. P. Colomban, J.M. Herrera Ramirez, R. Paquin, A. Marcellan and A. Bunsell, *Eng. Fract. Mechan.*, **73**, 2463-2475 (2006).

39. P. Colomban, *Compo. Sci. Tech.*, **69**, 1437-1441 (2009).

40. C. Galiotis, *Mater. Tech*., **8**, 203-209 (1993)

41. P.J. Hendra and W.F. Maddams, In *Polymer Spectroscopy*, John Wiley & Sons, A.H. Fawcett, Chichester (1996)

42. J.C. Rodriguez-Cabello, J.C. Merino and J.M. Pastor, *J. Raman Spec.*, **27**, 463-467 (1996).

43. R.J. Young and S.J. Eichorn, *Polymer*, **48**, 2-18 (2007).

44. J. Purvis and D.I. Bower, *J. Polym. Sci.*, **14**,1461-1484 (1976).

45. M. Tanaka and R.J. Young, *J. Mater. Sci.*, **41**, 963-991 (2006).

46. B. Wunderlich, *Macromolecular Physics: Crystal structure, Morphology, Defects*, Academic Press, New York (1973).

47. B. Lotz and J.C. Wittman, *J. Polym. Sci*., **24**, 1541-1558 (1986).

48. F. Addiego, A. Dahoun, C. G'Sell and J.M. Hiver, *Polymer*, **47**(12), 4387-4399 (2006).

49. K. Levenberg, *Quart. Appl. Math*., **2**, 164-168 (1944).

50. J.C. Viana, A.M. Cunha and N. Billon, *Polym. Eng. Sci.*, **39**(8), 1463-1472 (1999).

51. J. Martin, *Ph. D. Thesis*, Université Paul Verlaine Metz, France (2009).

52. M. Ponçot, *Ph. D., Thesis*, Institut National Polytechnique de Lorraine, Nancy, France (2009).

53. J. Martin, S. Margueron, M. Fontana, M. Cochez and P. Bourson, *Polym. Eng. Sci*., **50**, 138-143 (2010) .

54. J. Martin, P. Bourson, A. Dahoun and J.M. Hiver, *Appl. Spec.*, **63**, 1377-1381 (2009).

55. M. Ponçot, J. Martin, J.M. Hiver, D. Verchère, A. Dahoun, , *J. Appl. Polym. Sci.*, 125(5), 3385-3395 (2012)

56. J. Martin, M. Ponçot, P. Bourson, A. Dahoun, J.M. Hiver, *Polym. Eng. Sci.*, 51(8), 1607-1616 (2011)

57. R.G. Snyder and J.H. Schachtshneider, *Spectrochim. Acta A*, **20**, 853-869 (1964).

58. H. Tadokoro, M. Kobayashi, M. Ukita, K. Yasufuku, S. Murahashi and T. Torii, *J. Chem. Phys.*, **42**(4), 1432-1448 (1965).

59. G. Zerbi and L. Piseri, *J. Chem. Phys*, **49**, 3840 (1964).

60. G.V. Fraser, P.J. Hendra, D.S. Watson, M.J. Gall, H.A. Willis and M.E.A. Cudby, *Spectrochim. Acta A*, **29**, 1525-1533 (1972).

61. J.M. Chalmers, H.G.M. Edwards, J.S. Lees, D.A. Long, M.W. Mackenzie and H.A. Willis, *J. Raman Spec.*, **22**(11), 613-618 (1991).

62. T.C. Damen, S.P.S. Porto and B. Tell, *Phys. Rev.*, **142**(2), 570-574 (1966).

63. C. G'Sell, A Dahoun,V. Favier, J.M. Hiver, M.J. Philippe and G.R. Canova, *Polym. Eng. Sci*., **37**, 1702-1711, (1997).

64. R.P. Wool, R.S. Bretzlaff, B.Y. Li, Wang C.H., Boyd R.H.,J. Polym. Sci., 24, 1039-1066 (1985)

65. J.M. Haudin, In *Plastic Deformation of Amorphous and Semi Crystalline Materials*, B. Escaig and C. G'Sell, Les Editions de Physique, Les Ullis, 291-311 (1982).

66. M. Aboulfaraj, C. G'Sell, B. Ulrich, A. Dahoun, Polymer, 36, 731-742 (1995).

67. G. Castelein, G. Coulon, C. G'Sell, Polym. Eng. Sci., 37, 1694-1701 (1997).

68. Dijkstra P.T.S., Van Dijk D.J., Huetink J., Polym. Eng. Sci., 42, 152-160 (2002)

69. E. Weynant, J.M. Haudin, C. G'Sell, *J. Mater. Sci.,* **15**, 2677-2692 (1980).

70.E.J. Kramer, In *Plastic Deformation of Amorphous and Semi Crystalline Materials*, B. Escaig and C. G'Sell, Les Editions de Physique, Les Ullis, 391-405 (1982).

List of tables

Table1 : Vibrational and phase assignments for Raman scattering bands of iPP. From Ref. [51-61]

Table 2 : Raman spectroscopy results on major microstructural aspects of iPP uniaxially stretched at T = 30 °C under a constant true strain rate $\dot{\varepsilon}_{zz}$ = 5.10^{-3} s^{-1} from the elastic to the stress-hardening regime.

Table 1 : Vibrational and phase assignments for Raman scattering bands of iPP. From Ref. [51-61]

Position ν (cm^{-1})	**Intensity**	**Assignment**	**Phase**
809	strong	ν_s(C-C), r(CH2)	Crystalline (60 %) Amorphous (40 %)
835	medium	ν_s(C-C)	Amorphous
842	strong	r(CH2)	Crystalline (65 %) Amorphous (35 %)
973	strong	ν_{as}(C-C), r(CH_3)	Crystalline
998	strong	r(CH_3)	Crystalline

Table 2 : Raman spectroscopy results on major microstructural aspects of iPP uniaxially stretched at T = 30 °C under a constant true strain rate $\dot{\varepsilon}_{zz}$ = 5.10^{-3} s^{-1} from the elastic to the stress-hardening regime.

		deformation regime		
microstructural aspect	descriptive parameter	**elasto-viscoelastic regime 0.00 - 0.09**	**soft-plastic regime 0.09 - 0.80**	**stress-hardening regime 0.80 - 1.60**
crystallinity index	$<X_c>$	0.67 - 0.67	0.67 - 0.57	0.57 - 0.54
crystalline phase orientation	$F_{C/Z}$	0.05 - 0.05	0.05 - 0.48	0.48 - 0.74
amorphous phase orientation	$F_{am/Z}$	0.03 - 0.30	0.30 - 0.60	0.60 - 0.70
stress on C-C cryst.bonds	ν_{809}/ν_{809}^0	1.0000 - 1.0000	1.0000 - 0.9995	0.9995 - 0.9980
stress on C-C amor. bonds	ν_{835}/ν_{835}^0	1.0000 - 0.9990	0.9990 - 0.9985	0.9985 - 0.9960
stress on C-H cryst. bonds	ν_{842}/ν_{842}^0	1.0000 - 1.0000	1.0000 - 1.0005	1.0005 - 1.0020

List of figures

Figure 1: (a**)** Depolarized Raman spectra and **(**b**)** fitted scattering bands at 809, 835 and 842 cm^{-1} of iPP stretched at different strain levels.

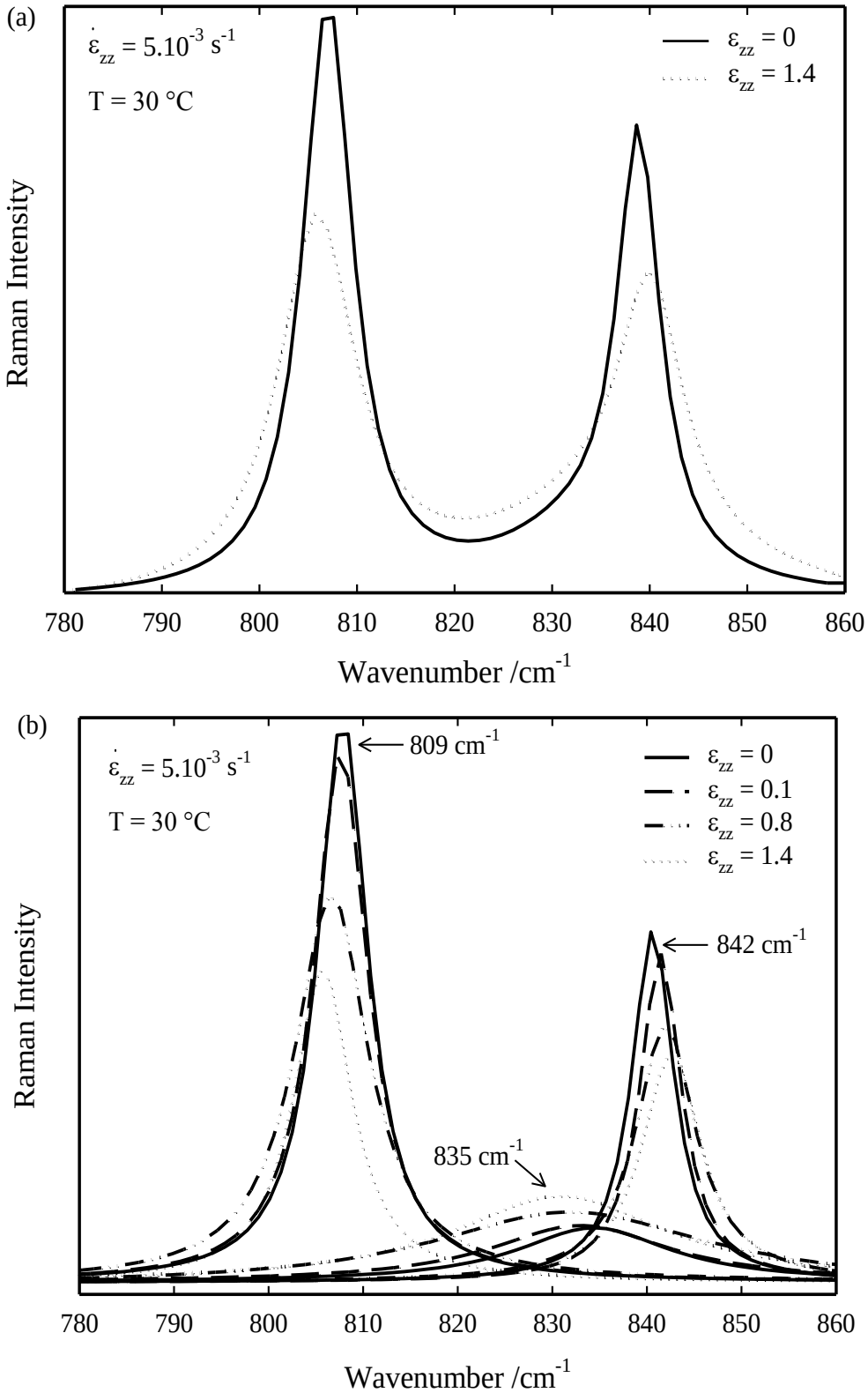

Figure2 : Evolution of the true axial stress, σ_{zz}, and the crystallinity index, $<X_c>$, in function of the true axial strain, ε_{zz}, of iPP uniaxially stretched at T = 30 °C under a constant true strain rate $\dot{\varepsilon}_{zz} = 5.10^{-3}\ s^{-1}$.

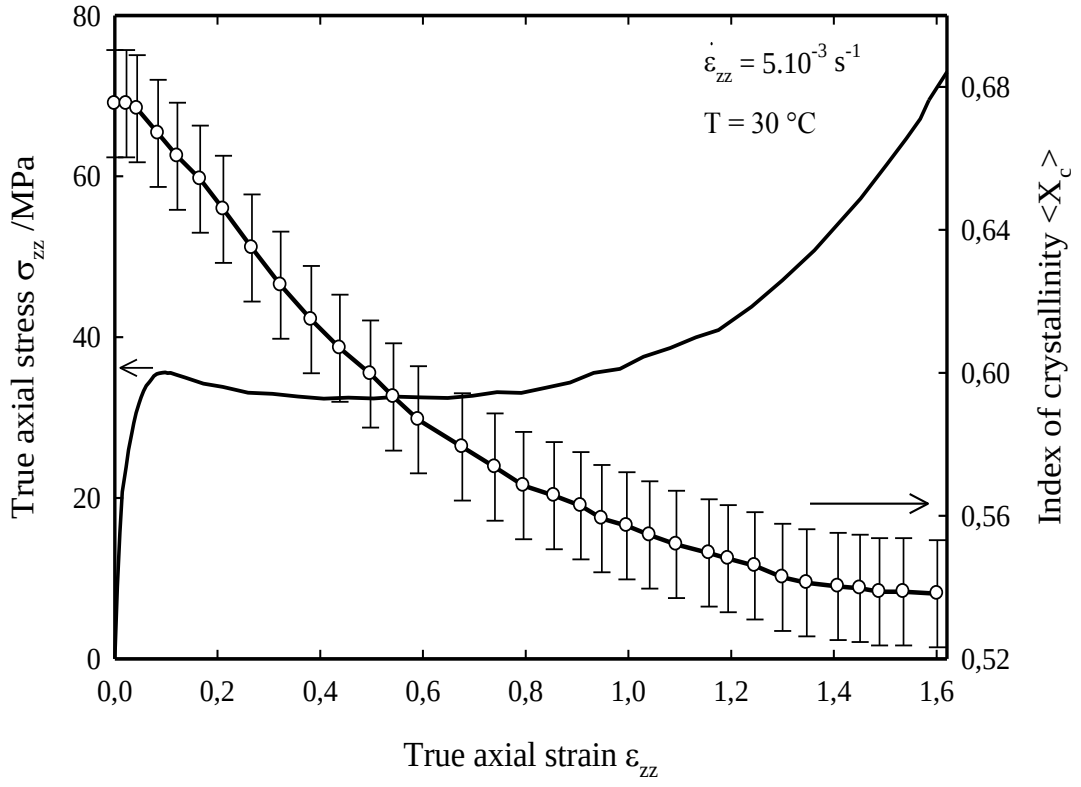

Figure3 : (a**)** Polarized **x(zz)x** Raman spectra and **(**b) fitted scattering bands at 973 and 998 cm^{-1} of iPP stretched at different strain levels.

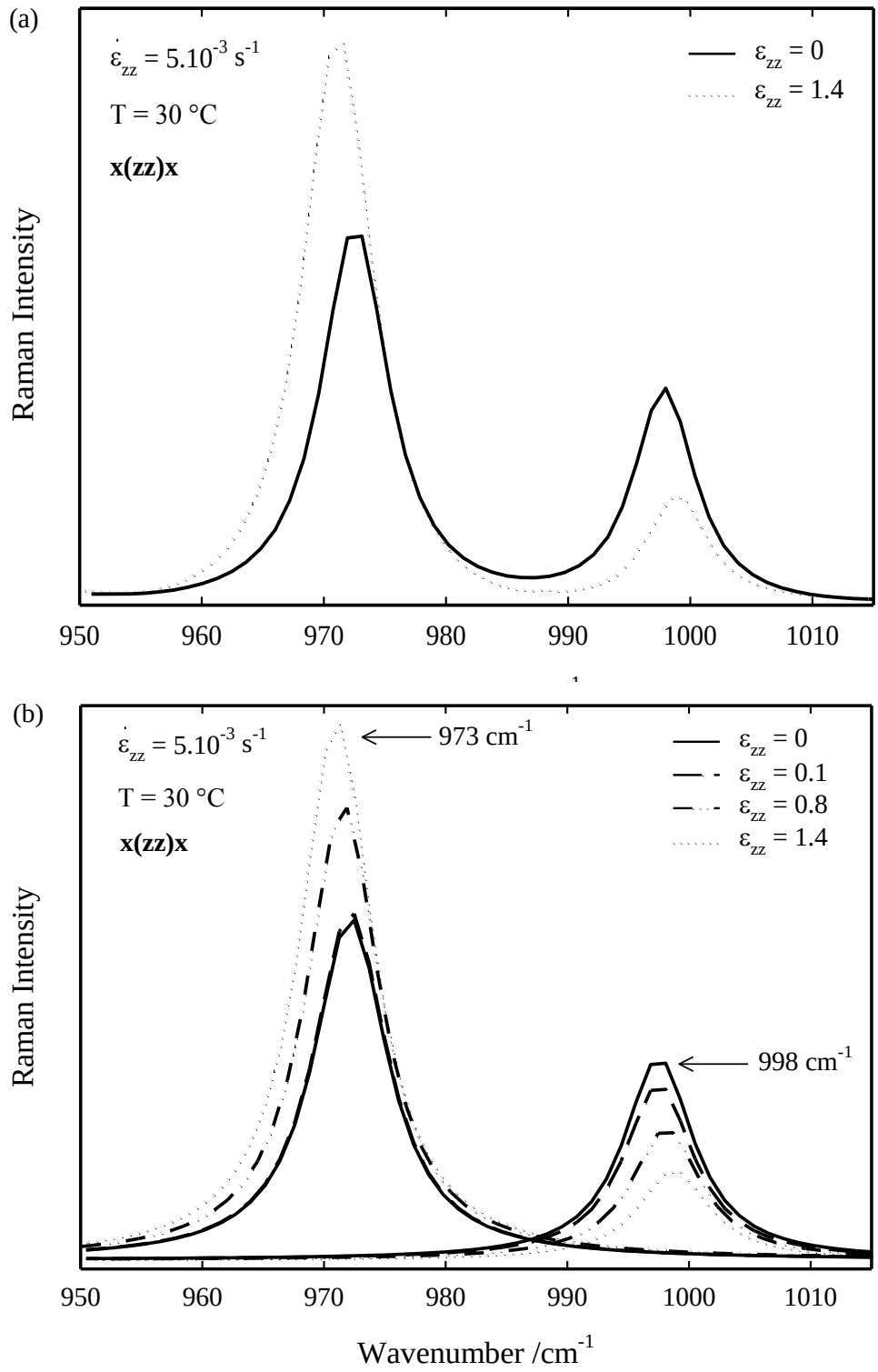

Figure 4 : Evolution of the true axial stress, σ_{zz}, and the orientation function of the crystalline phase, $F_{c/z}$, in function of the true axial strain, ε_{zz}, of iPP uniaxially stretched at T = 30 °C under a constant true strain rate $\dot{\varepsilon}_{zz}$ = 5.10^{-3} s^{-1}.

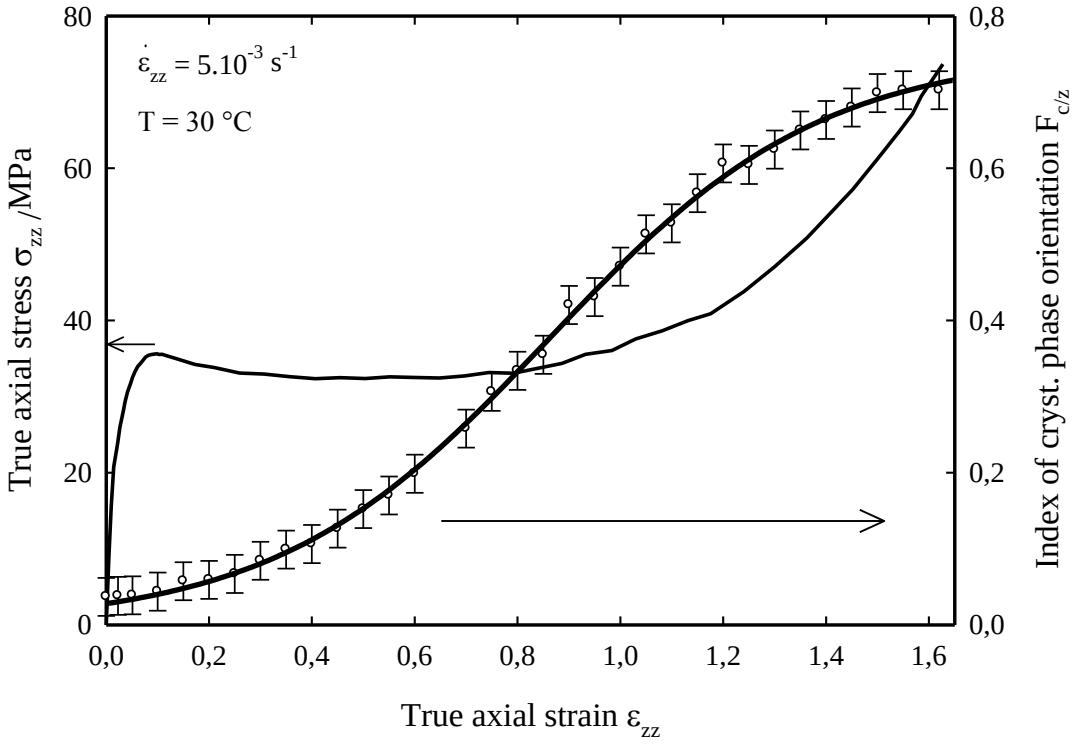

Figure 5 : Fitted Raman scattering band at 835 cm^{-1} for different strain levels of iPP recorded in the **x(zz)x** polarized light configuration.

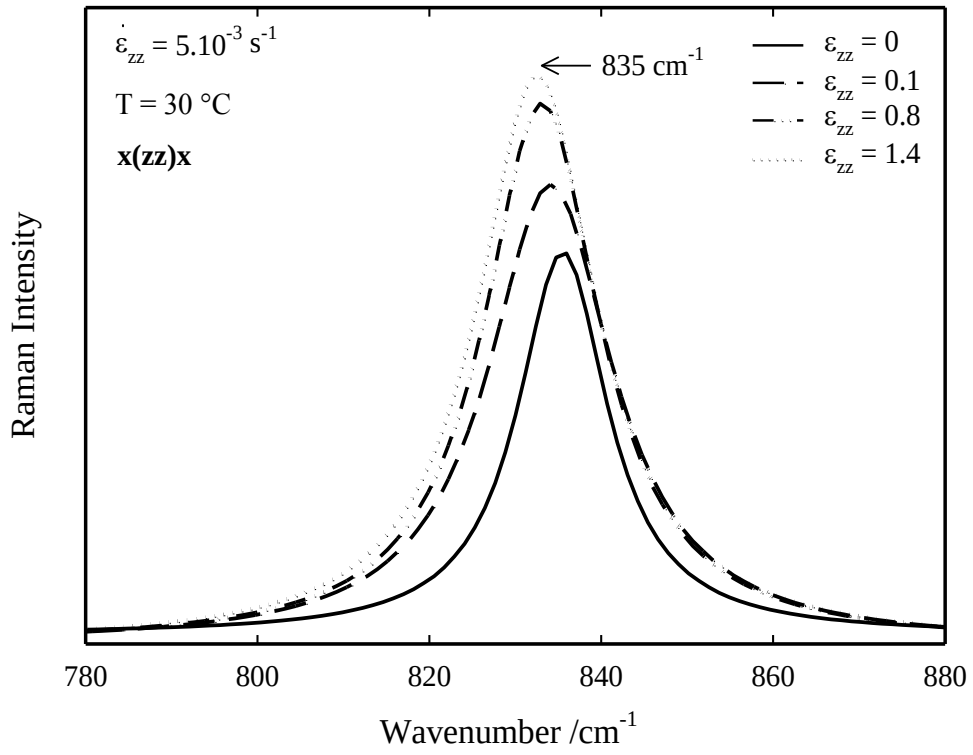

Figure 6 : Evolution of the true axial stress, σ_{zz}, and the orientation function of the amorphous phase, $F_{am/z}$, in function of the true axial strain, ε_{zz}, of iPP uniaxially stretched at T = 30 °C under a constant true strain rate $\dot{\varepsilon}_{zz}$ = 5.10^{-3} s^{-1}.

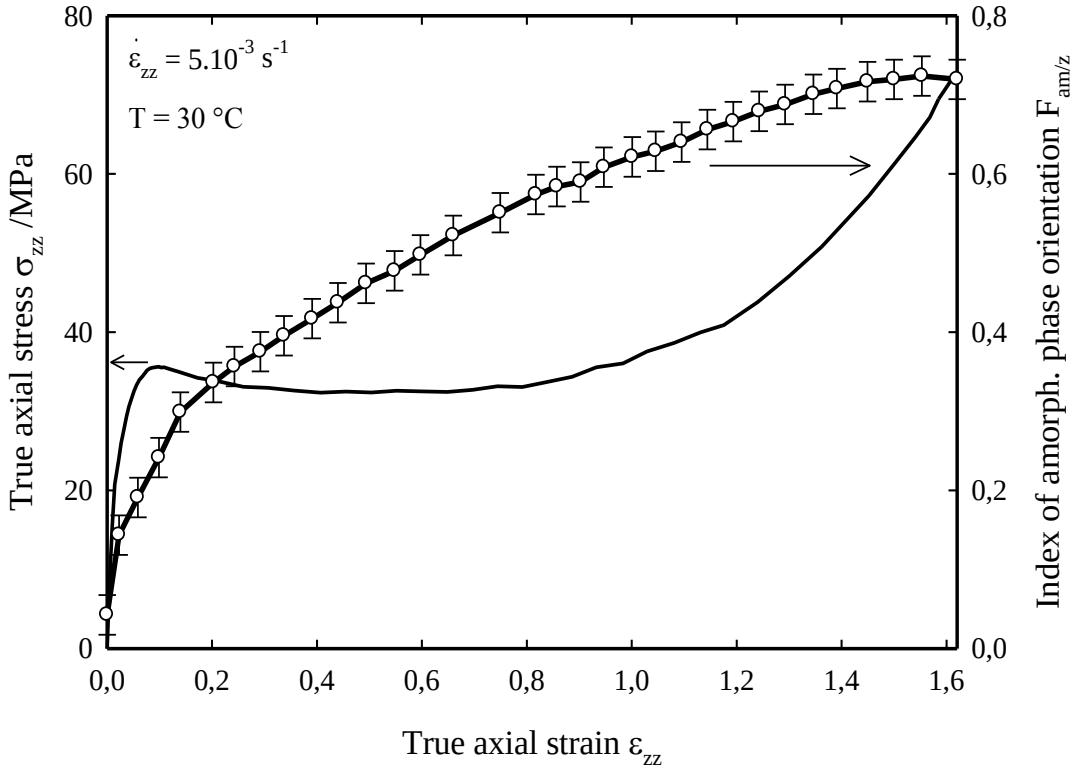

Figure 7 : Evolution of the true axial stress, σ_{zz}, and the normalized position, ν / ν^0, of crystalline bands at 809 (C-C) and 842 cm^{-1} (CH_2)

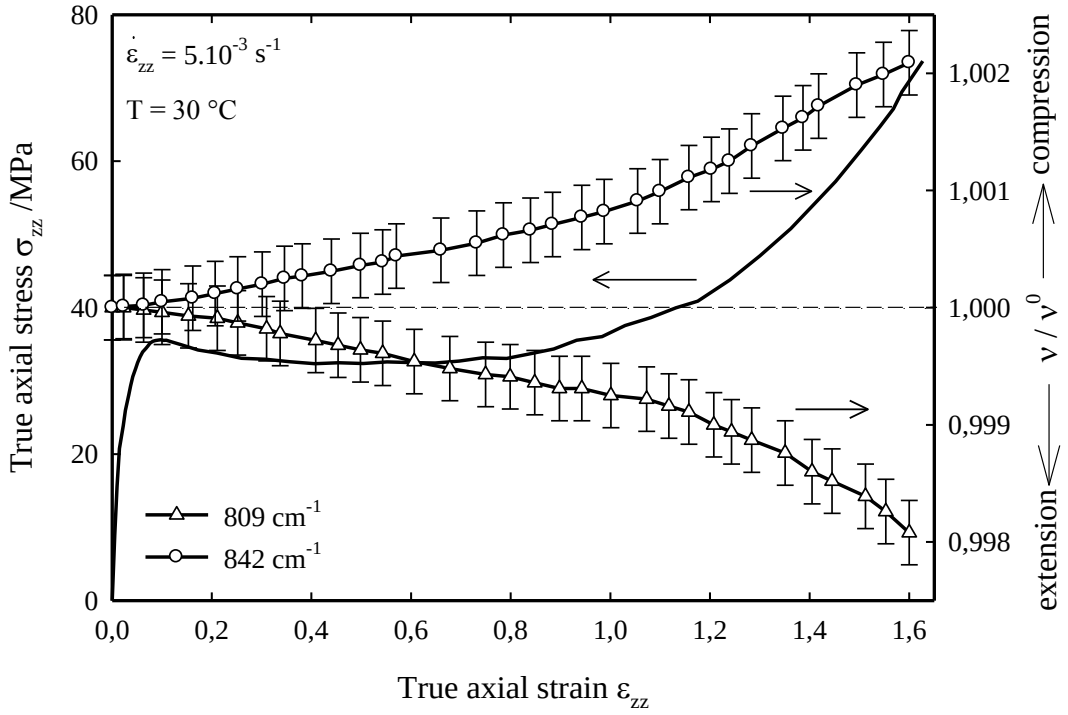

Figure 8 : Evolution of the true axial stress, σ_{zz}, and the normalized position, ν / ν^0, of amorphous band at 835 cm^{-1} (C-C) in function of the true axial strain, ε_{zz}, of iPP uniaxially stretched at T = 30 °C under a constant true strain rate $\dot{\varepsilon}_{zz} = 5.10^{-3}\ s^{-1}$.

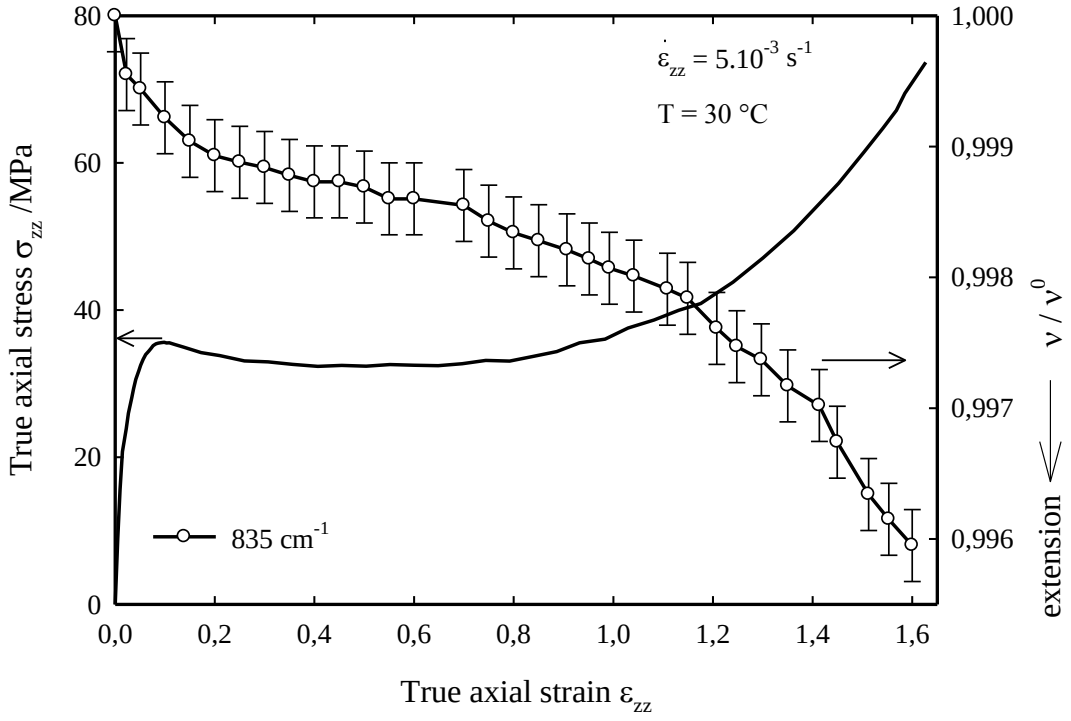

Figure 9 : A schematic illustration of micro-structural mechanisms occurring in uniaxially stretched iPP during the initial elasto-viscoelastic regime, the soft-plastic deformationregime and the stress-hardening regime.